Physics of Fluids

Mechanism of end-gas autoignition induced by flame-pressure interactions in confined space

Cite as: Phys. Fluids **31**, 076106 (2019); https://doi.org/10.1063/1.5099456
Submitted: 10 April 2019 . Accepted: 30 June 2019 . Published Online: 24 July 2019

Haiqiao Wei (卫海桥), Xiaojun Zhang (张晓军), Hao Zeng (曾昊), Ralf Deiterding, Jiaying Pan (潘家营), and Lei Zhou (周磊)

Physics of Fluids ARTICLE scitation.org/journal/phf

Mechanism of end-gas autoignition induced by flame-pressure interactions in confined space

Cite as: Phys. Fluids 31, 076106 (2019); doi: 10.1063/1.5099456
Submitted: 10 April 2019 • Accepted: 30 June 2019 •
Published Online: 24 July 2019

Haiqiao Wei (卫海桥),[1] Xiaojun Zhang (张晓军),[1] Hao Zeng (曾昊),[2] Ralf Deiterding,[3] Jiaying Pan (潘家营),[1] and Lei Zhou (周磊)[1,a)]

AFFILIATIONS

[1] State Key Laboratory of Engines, Tianjin University, Tianjin 300072, China
[2] Aeronaustics Enginneering College, Airforce Enginneering University, Xi'an 710051, China
[3] Aerodynamics and Flight Mechanics Research Group, University of Southampton, Highfield Campus, Southampton SO171BJ, United Kingdom

[a)] **Author to whom correspondence should be addressed:** lei.zhou@tju.edu.cn. **Tel.:** +86-022-27402609.

ABSTRACT

The main objective of this work is to comprehensively provide a fundamental understanding of the entire process of the flame-pressure wave interactions with end-gas autoignition and detonation development in a confined chamber by two-dimensional numerical simulations with a stoichiometric hydrogen/air mixture. The flame dynamics, pressure wave propagation, and its structure evolution, together with the mechanism of autoignition and detonation development in the end gas, are analyzed in detail. Six stages, including spherical flame, finger flame, flame with its skirt touching the sidewalls, flame-pressure wave interactions, end-gas autoignition induced by the flame-pressure wave interactions, and detonation development, are observed for the flame development in the confined space. The results demonstrate that the flame-pressure wave multi-interactions result in violent oscillations of the flame shape and speed. Three stages of flame shape evolution during each interaction, backward propagation of the flame front, stretch of the flame front at the boundary layer, and formation of the tulip flame, are captured. A new mechanism in terms of combined effects of the viscous boundary layer and pressure waves is provided for the formation of the tulip flame. It is also found that the velocity distributions in the boundary layer show the trend of increase first and then decrease after the pressure waves pass the fields twice in the opposite directions. The autoignition occurrence and detonation initiation at different positions and different moments in the end-gas region are analyzed. It is indicated that the nonuniform temperature distribution induced by the reflections of pressure waves and the specific pressure wave structures can be responsible for this phenomenon.

I. INTRODUCTION

Flame propagation and deflagration-to-detonation transition (DDT) have drawn extensive attention over the past years not only due to their destructive effects in the fire safety area such as mine explosion but also because of their potential applications in some propulsion systems, e.g., a pulsed detonation engine (PDE).[1–8] It is generally considered that the overall DDT process in a smooth tube basically involves three stages: first, flame acceleration and leading shock wave generation, then formation of the preheated zone ahead of the flame front, and finally, formation of a detonation wave (DW).[8,9] However, the quantitative theory and comprehensive mechanism of DDT remain still poorly understood as a result of its complicated combination of multiple highly nonlinear processes including interactions among flames, shocks, boundary layers, and turbulence.[2] In particular, detonation development in confined space has become a new forefront topic recently on account of its close relation to superknock occurring in downsized spark ignition engine,[10–15] in which the complex flame-pressure wave interactions play a crucial role in the end-gas autoignition formation and its inducing detonation.[12–14] When superknock occurs, the peak pressure in the cylinder can reach up to over 300 bars that can damage the engine, which has become an obstacle for the development of an advanced engine. Thus, understanding the mechanism of flame-pressure/shock wave interactions in the confined space not only is of fundamental significance for detonation theory but also contributes to the practical applications for suppression of knock.

In recent decades, there have been a number of studies on the interactions between flame propagation and pressure/acoustic/shock waves through experiments and simulations. As early as 1956, Markstein[16] investigated the interaction of initially laminar flames with shock waves, which showed that the interaction of the flame with the shock wave leads to the formation of a spike of unburned gas that penetrates rapidly into burned gas. Later, Searby[17] presented an experimental description of the acoustic instability of a premixed flame front in a tube with a closed end, where four distinct types of acoustic instability in terms of the oscillation of acoustic wave and flame structures are included. Bychkov[18,19] developed analytical models describing stabilization and destabilization of curved flames during interactions with weak shocks or acoustic waves in tubes. Afterward, Petchenko *et al.*[20,21] numerically showed that flame-sound interactions strongly increase the oscillation amplitude of the flame front and that oscillations become especially strong when flame pulsations are in resonance with the acoustic wave. Recently, Akkerman and Law[22] analytically investigated the acoustic wave-flame interactions in spherical confinement and found that the acoustics modify the power-law flame acceleration, concomitantly facilitating or inhibiting the transition to detonation in confinement. Apart from the oscillations, flame shape changes caused by flame-pressure/acoustic/shock wave interactions are one of the most interesting parts because of its close relation to flame acceleration that can lead to DDT. Clanet[23] studied the tulip flame phenomenon in a half-open tube and noted that the formation of the tulip flame is a manifestation of the Taylor instability driven by the deceleration of the flame tip. In recent works,[24–26] experimental and numerical investigations were performed to study a new flame shape, called "distorted tulip" flame (DTF), which appears after a classical tulip flame is formed. In these works, Xiao *et al.*[25] suggested that the formation of a DTF is the result of Rayleigh–Taylor instability (RTI) driven by pressure waves generated by contact of the flame front with the sidewalls. Meanwhile, shock-flame bubble interactions in terms of Richtmyer–Meshkov Instability (RMI) are also extensively investigated.[27–30] Thomas *et al.*[27] experimentally observed that increased incident shock velocity results in enhancement of combustion and deflagration to detonation transition. Zhu *et al.*[29] numerically studied effects of different parameters on spherical flame-shock interactions and showed that the time-dependent integral and statistical properties of flame developments prior to detonation onset show more similar behaviors compared to the spatial dissimilarities of flame and detonation evolution for all cases. All these previous studies have significantly improved our understanding of the flame-pressure/acoustic/shock wave (all stated as pressure wave below) interactions. However, the effects of the flame-pressure wave interactions on the autoignition and detonation development in the end-gas region have not been investigated in these works.

Meanwhile, significant efforts have been spent on studying autoignition due to its close association with knock and superknock. Zeldovich[31] first presented that there are different combustion modes for a flame front propagation caused by autoignition in the mixture with nonuniform reactivity. Based on the above theory, Bradley and his co-workers[32–34] extended these studies and further developed an operational peninsula, where two nondimensional parameters, ξ and ε, representing the acoustic speed normalized by the autoignition velocity and the acoustic wave residence time in a hotspot normalized by the excitation time, respectively, are involved. This peninsula can be adopted to classify different combustion regimes with clear regime boundaries in terms of autoignition mode during knocking combustion. In addition, a number of experimental studies have been performed to investigate the autoignition and knock. Using the rapid compression machine (RCM) with an optical window,[10,35,36] it was observed that detonation is first initiated in the near-wall region as a result of shock wave reflection and Wang *et al.*[35] demonstrated that the mechanism of superknock is constituted by hotspot-induced deflagration to detonation transition followed by high-pressure oscillation. However, pressure waves and especially flame-pressure wave interactions were not observed directly in the experiments. Thus, Wei *et al.*[13,37] conducted experiments in a constant volume combustion chamber with schlieren photography. It is shown that the interaction of the reflected shock wave and flame results in oscillations of the flame propagation and the end-gas autoignition induced by the shock waves was captured as well.

Moreover, significant advances have been made over the past years in the simulations of autoignition and engine knock,[12,38–44] especially by one-dimensional (1D) computations. Terashima and Koshi[41] conducted a 1D simulation to deal with the mechanism for the hot-spot formation. The results demonstrated that the wall reflection periodic of the compression wave, generated from spark, produces an instantaneous temperature increase, which leads to the production of a larger amount of chemical species compared to that of other end-gas points. Furthermore, Yu and Chen[44] observed three different modes of end-gas combustion: normal flame (NF) propagation without autoignition, autoignition without detonation development, and detonation development. They also pointed out that autoignition and detonation development can be induced by increasing the initial temperature, initial pressure, or chamber length. However, due to the limits of 1D simulation, the flame dynamics and the generation and propagation of pressure waves due to the flame acceleration, which are of great importance in the process of real knocking combustion, were not observed.

The main objective of the present study is to provide a fundamental understanding of the integrated process of the flame-pressure wave interactions with end-gas autoignition and detonation development in the confined space. The discussions are based on the results of a set of two-dimensional (2D) simulations with a stoichiometric hydrogen–air mixture, in which the compressible Navier–Stokes equations are solved with a reduced chemical kinetics mechanism of H_2. The new contributions of the present work are the following: (1) Different flame propagation modes and flame dynamics in a confined chamber are presented by 2D simulations, for the first time to our best knowledge. The oscillations of the flame speed and evolution of the flame shape, caused by the interactions of flame and pressure waves in a confined chamber, are comprehensively discussed in this work. (2) The generation and propagation of the pressure waves in the confined space by the wave diagram as well as their structure evolution during interactions with the flame front are carefully investigated. Also, a new mechanism in terms of combined effects of the viscous boundary layer and the pressure waves is performed for the formation of the tulip flame. (3) The mechanism of end-gas autoignition with detonation development induced by the flame-pressure wave interactions is revealed comprehensively. The present work will give deep insight into the mechanism of end-gas autoignition as well as the DDT phenomenon.

The paper is organized as follows: the computational configurations and numerical methods are briefly discussed in Sec. II. The results and discussions are presented in Sec. III, where the flame dynamics and pressure wave propagation as well as the analysis of autoignition and detonation development are included. Finally, major conclusions from this work are summarized in Sec. IV.

II. COMPUTATIONAL CONFIGURATIONS AND NUMERICAL METHODS

A. Computational configurations

As shown in Fig. 1, the 2D closed rectangular channel, whose length and height are denoted as $l = 2$ cm and $d/2 = 0.1$ cm, respectively, is considered in the present work. To reduce computation expenses, a symmetric boundary condition is adopted at the lower boundary, while adiabatic and reflective no-slip boundary conditions are imposed at the other three sides. Note that in this work, the effects of wall heat losses on the flame propagation are not considered based on similar studies[45,46] to improve computational efficiency. Initially, an artificial hot kernel is set up at the lower side close to the left wall ($X = 0.1$ cm), as the spark ignition kernel, surrounded by a quiescent homogeneous stoichiometric H_2/air mixture with the initial temperature of $T_0 = 1000$ K and the initial pressure of $P_0 = 10$ bars. The initial distributions for temperature and mass fractions of all species inside the hot kernel are extracted from the results computed by the Premix laminar flame-speed calculation model in Chemkin-PRO[47] for stoichiometric H_2/air at T_0 and P_0. A flame front induced by the hot kernel will propagate from left to right and detonation induced by autoignition may take place in the end-gas region between the flame front and the right wall in conjunction with the pressure and temperature increase. A reduced reaction mechanism of Li *et al.*[48] for the H_2/air mixture is utilized in the present work. Note that the dimensions considered here are often applied in the studies of flame propagation in a microscale or narrow channel[6,46,49] where heat losses to the wall can have a non-negligible impact on the flame propagation,[2,50,51] but the present work is mainly focused on the fundamental mechanism of flame-pressure wave interactions and their effects on the end-gas autoignition and detonation development in confined space under a high temperature (HT) and pressure condition, and the potential effects of heat losses are only roughly discussed for the integrity while the detailed mechanism needs to be further investigated in the future. In addition, effects of initial temperature T_0, initial pressure P_0, and lager channel dimensions are also investigated, and the results are provided in Subsections 1 and 2 of the Appendix for highlighting the slight process differences between these cases.

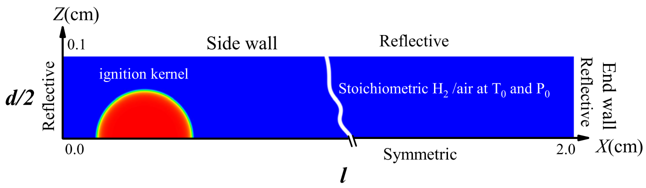

FIG. 1. Computational model.

B. Governing equations

The reactive compressible Navier–Stokes equations are used for the governing equations, which are expressed as follows:

$$\frac{\partial \boldsymbol{U}}{\partial t} + \frac{\partial(\boldsymbol{F_{conv}} - \boldsymbol{F_{diff}})}{\partial x} + \frac{\partial(\boldsymbol{H_{conv}} - \boldsymbol{H_{diff}})}{\partial y} = \boldsymbol{S_{chem}}, \tag{1}$$

$$\boldsymbol{U} = (\rho, \rho u, \rho v, \rho e_t, \rho_1, \ldots, \rho_{K-1})^T, \tag{2}$$

$$\boldsymbol{S_{chem}} = (0, 0, 0, 0, \dot{\omega}_1, \ldots, \dot{\omega}_{K-1})^T, \tag{3}$$

$$\boldsymbol{F_{conv}} = \begin{pmatrix} \rho u \\ \rho u^2 + p \\ \rho u v \\ (\rho e_t + p)u \\ \rho_1 Y_1 u \\ \vdots \\ \rho_{K-1} Y_{K-1} u \end{pmatrix}, \quad \boldsymbol{F_{diff}} = \begin{pmatrix} 0 \\ \tau_{xx} \\ \tau_{xy} \\ u\tau_{xx} + v\tau_{xy} - q_x \\ \rho_1 Y_1 V_{x,1} \\ \vdots \\ \rho_{K-1} Y_{K-1} V_{x,K-1} \end{pmatrix},$$
$$\boldsymbol{H_{conv}} = \begin{pmatrix} \rho v \\ \rho u v \\ \rho v^2 + p \\ (\rho e_t + p)v \\ \rho_1 Y_1 v \\ \vdots \\ \rho_{K-1} Y_{K-1} v \end{pmatrix}, \quad \boldsymbol{H_{diff}} = \begin{pmatrix} 0 \\ \tau_{yx} \\ \tau_{yy} \\ u\tau_{yx} + v\tau_{yy} - q_y \\ \rho_1 Y_1 V_{y,1} \\ \vdots \\ \rho_{K-1} Y_{K-1} V_{y,K-1} \end{pmatrix}. \tag{4}$$

Here, ρ, u, v, e_t, p, ρ_i, $\dot{\omega}_i$, Y_i, $V_{x,i}$ and $V_{y,i}$ are the total density, the velocity in the x-direction, the velocity in the y-direction, the total energy per unit mass, the pressure, the density of the ith species, the mass production rate of the ith species, the mass fraction of the ith species, the diffusion velocity in the x-direction of the ith species, and the diffusion velocity in the y-direction of the ith species, respectively.

The viscous stress tensor is given by

$$\tau_{xx} = \mu\left(\frac{4}{3}\frac{\partial u}{\partial x} - \frac{2}{3}\frac{\partial v}{\partial y}\right), \quad \tau_{xy} = \tau_{yx} = \mu\left(\frac{\partial v}{\partial x} + \frac{\partial u}{\partial y}\right),$$
$$\tau_{yy} = \mu\left(\frac{4}{3}\frac{\partial v}{\partial y} - \frac{2}{3}\frac{\partial u}{\partial x}\right). \tag{5}$$

The heat flux is assumed to obey Fourier's law, and its dependence on interspecies diffusivities is fully considered,

$$q_x = -k\frac{\partial T}{\partial x} - \rho\sum_{i=1}^{K} h_i D_i \frac{\partial Y_i}{\partial x}, \quad q_y = -k\frac{\partial T}{\partial y} - \rho\sum_{i=1}^{K} h_i D_i \frac{\partial Y_i}{\partial y}, \tag{6}$$

where h_i is the enthalpy of the ith species and T is the temperature. The contribution of each species to the total energy is obtained by using a mass fraction averaged enthalpy,

$$h = \sum_{i=1}^{K} Y_i h_i, \tag{7}$$

where

$$h = e_t + \frac{\rho}{p} - \frac{u^2 + v^2}{2}. \tag{8}$$

The dynamic viscosity μ, thermal conductivity k, and mass diffusion coefficients D_i are evaluated by the Chemkin-II library[52] linked to AMROC.

Finally, the perfect gas equation of state is used to close the equations

$$p = \rho R \sum_{i=1}^{K} \frac{Y_i}{W_i} T, \tag{9}$$

where R is the universal gas constant and W_i is the molar mass of each species.

C. Numerical methods

The parallel adaptive mesh refinement framework Adaptive Mesh Refinement in Object-oriented C++ (AMROC)[53–55] based on the Structured Adaptive Mesh Refinement (SAMR) approach[56] has been adopted to solve the reactive compressible Navier–Stokes equations. The time-operator splitting approach is utilized to decouple hydrodynamic transport and chemical reaction source term numerically by using Godunov splitting. This technique is most frequently used for time-dependent reactive flow computations. The fifth-order accurate weighted essentially nonoscillatory (WENO) scheme is applied for discretization of the convective part of the NS equations, while the sixth-order accurate Central Difference (CD) scheme is used for the diffusion terms and the third-order Runge-Kutta scheme is used for the temporal integration. The reactive source term is solved by the VODE solver[57] within each cell. With the adaptive mesh refinement method, AMROC can accurately resolve the flame front, shock wave, and detonation, and thus has been successfully applied to the extensive studies of combustion.[53,58–62]

D. Grid convergence

As shown in Fig. 2, four level refinement with refinement factors (2, 2, 2) is adopted in the present work, which can give the finest mesh with the size of 3.125 μm by using the base mesh size of 25 μm, corresponding to more than 10 cells per flame thickness and 7 cells per induction length under current initial conditions. With the appropriate refinement criterion, the flame, pressure waves, and boundary layer are completely covered by the finest mesh so that they can be adequately resolved. In addition, the verification of grid convergence is conducted with three different minimum mesh sizes, including 6.25 μm, 3.125 μm, and 1.5625 μm, while the base cell size keeps 25 μm. Figure 3 shows the temporal evolution of the flame tip position (FTP) and pressure at the point (X = 2.0 cm, Z = 0 cm) with these three mesh sizes. The results indicate that a grid converged solution is achieved with the finest mesh size of 3.125 μm and 1.5625 μm, while the mesh size of 6.25 μm produces a faster flame propagation and earlier autoignition, so the mesh size of 3.125 μm is adopted in the present work considering the computational expenses. Further validation of grid resolution can be found in Subsection 3 of the Appendix.

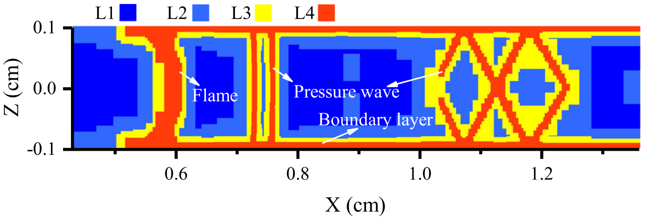

FIG. 2. Adaptive mesh refinement of four levels with refinement factors (2, 2, 2), and the size of base mesh is 25 μm, which gives the finest mesh size of 3.125 μm.

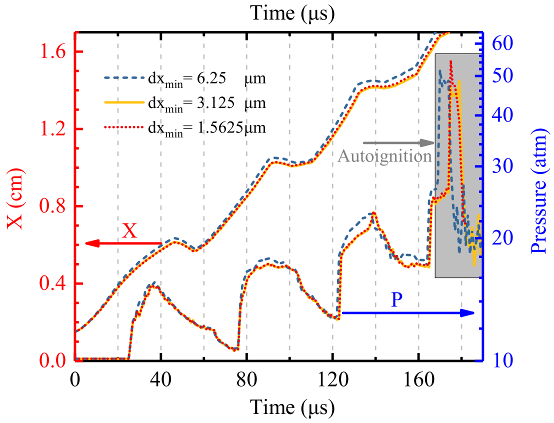

FIG. 3. Temporal evolutions of the flame tip position and pressure at the point (x = 2, z = 0) with three different minimum mesh sizes (dx_{min}), 6.25 μm, 3.125 μm, and 1.5625 μm, respectively. The gray rectangular indicates autoignition occurrence at the point.

III. RESULTS AND DISCUSSIONS

Figure 4 summarizes the entire process of flame propagation and detonation initiated by end-gas autoignition in the closed channel, which can be concluded in terms of six stages,

1. t = 0–3 μs, spherical flame;
2. t = 3–15 μs, finger flame;
3. t = 15–45.5 μs, flame with its skirt touching the sidewalls;
4. t = 45.5–174.8 μs, flame-pressure wave interactions;
5. t = 175 μs, end-gas autoignition induced by flame-pressure wave interactions; and
6. later, detonation initiation and development.

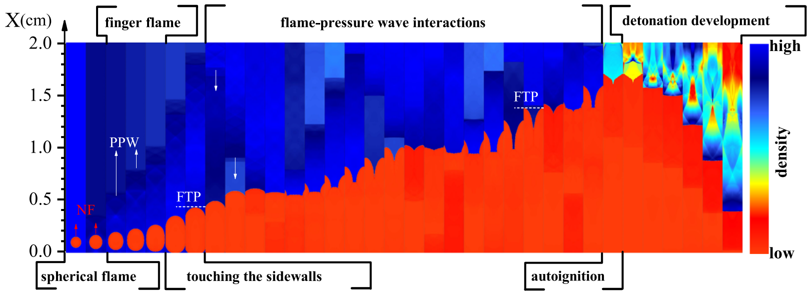

FIG. 4. Identification of six stages in the entire process of flame propagation and detonation development. NF-normal flame, PPW-primary pressure wave, FTP-flame tip position. Red and white arrows represent the propagation direction of normal flame and primary pressure wave, respectively.

It should be noted that between two contiguous images only the representative frames are selected to show flame propagation and detonation development. An overall description regarding the flame dynamics in the confined chamber is briefly presented here, and the detailed analysis will be discussed later. First, after initialization by the hot kernel, the flame expands spherically, unaffected by the sidewalls in the first stage. Then, the second stage occurs as the flame approaches the sidewalls and changes from spherical to finger shape due to the constraints of the walls. In the third stage, the flame expands continually and the lateral sides of the elongated flame touch the sidewalls, leading to the decrease of flame surface area. It should be noted that in the first three stages, flame configurations are in line with studies by Clanet[23] and Xiao *et al.*,[24–26] while at the following three stages significant combustion phenomena, induced by flame-pressure wave interactions in the confined chamber, are observed in the present study. The fourth stage occurs when the flame front meets the pressure wave generated by the flame acceleration and then reflected at the right wall. The pressure wave propagates backwards and forwards in the closed chamber and meets the flame front repeatedly, resulting in oscillations of the flame speed and shape. Consequently, autoignition occurs near the right end wall because of the increase in the local temperature and reactivity caused by the reflections of the pressure waves, and further results in the development of detonation, which propagates to the left and causes high frequency and intensity pressure oscillations in the chamber. In previous works,[13,23,25,35] only a partial process could be observed and the entire mechanism was not clearly understood until now. Therefore, this entire flame propagation with detonation occurrence in the confined space is reported in this work by 2D simulation, possibly for the first time.

A. Flame dynamics in the confined chamber

The profiles of flame tip position and flame speed as a function of time are shown in Figs. 5 and 6, respectively. Note that the flame tip is defined as the right most tip along the flame front. Generally, this tip is at the centerline at first three stages and coincides with the tip of tulip cusp at later stages (as discussed below), whose location is schematically identified by the dashed lines in Fig. 4. The flame tip position is defined as the distance from the flame tip location to the left side wall, and the flame speed is calculated based on the temporal derivative of the flame tip position. It is shown that in the first two stages the flame speed increases exponentially as the flame tip position is an exponential function of time, consistent with previous studies.[9,23,26,63] The flame acceleration is determined by the flame stretch. Basically, the flame expands at these two stages and especially at the second stage, the flame front extends along the x-direction continually because of the confinement of lateral walls, which extremely increases the flame surface area and thus results in faster energy release, consequently having a positive feedback on the

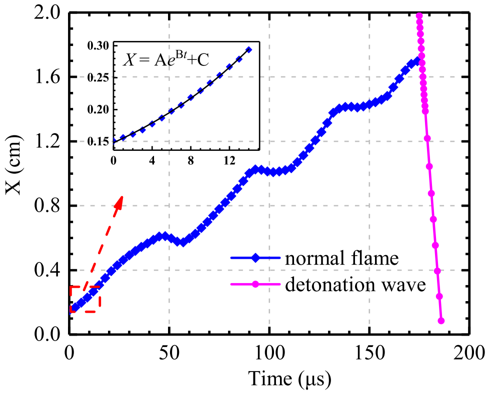

FIG. 5. Temporal evolutions of flame tip position (box-solid line) and detonation position (circle-solid line). The fitting formula is given in m-s units. Here, $A = 1.2 \times 10^{-3}$, $B = 5.6 \times 10^{4}$, $C = 2.6 \times 10^{-4}$.

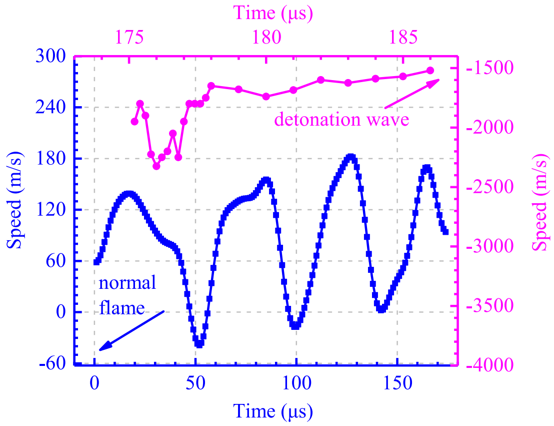

FIG. 6. Temporal evolutions of flame speed (box-solid line) and detonation speed (circle-solid line).

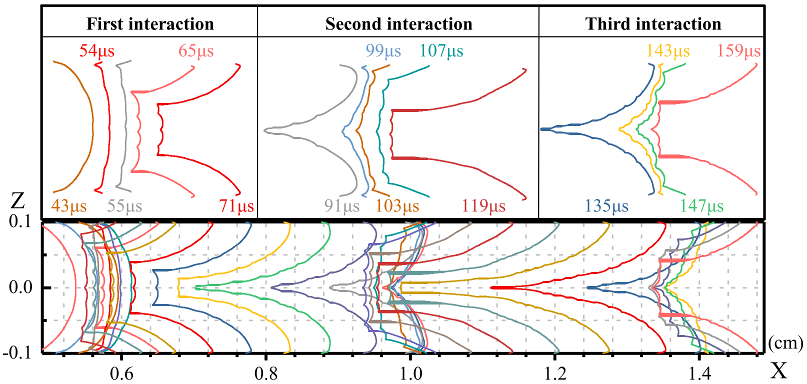

FIG. 7. Evolution of the flame front (isotherm at the temperature of 2000 K) during flame-pressure wave interactions at selected times.

flame speed.[9] Then, pressure waves are generated from the accelerating flame sequentially and overlap and coalesce with each other, leading to the increase in the pressure wave intensity and further to the development of the primary pressure wave, as shown in Fig. 4, which dominates the flame-pressure wave interactions in the current work, as discussed later. After the flame skirt touches the lateral sides at about 15 μs in the third stage, the flame quenches along the sidewalls due to the absence of fresh mixture and thus the flame surface area decreases, bringing about the deceleration of flame speed.

The primary pressure wave propagates to the left after being reflected by the right wall and consequently meets the flame front at about $X = 0.61$ cm when the fourth stage starts. Figure 7 shows the flame front evolution at this stage including three interactions of the flame and the primary pressure wave at selected times. For clear observation, the representative frames arranged in chronological order during three interactions are separately put on the upper half part in Fig. 7. The flame front evolution can be divided into three stages in terms of its development during each interaction: backwards propagation of the flame front, stretch of the flame front at the boundary layer, and formation of the tulip flame. Specifically, at the first stage, after meeting the primary pressure wave (not shown) propagating to the left, the flame front is strongly pushed back, which causes the flame front to nearly become flat, as shown from 43 to 54 μs. At the second stage, the flame front at the boundary layer is stretched gradually as a result of the contrary constraints between the no-slip wall and pressure waves propagating toward left, which causes the flame near the sidewalls move ahead of its rest part, as shown from 54 to 55 μs. Subsequently, the stretched flame near the walls is increasingly extended by the primary pressure wave propagating to the right after being reflected at the left wall at the last stage, which results in the development of two large cusps strongly moving toward right, as shown from 55 to 71 μs. The two cusps gradually draw close to the centerline and consequently the tulip flame forms as shown at 91 μs. Note that although it is a tulip flame not a finger flame that meets the pressure wave during the next two interactions, the overall flame shape evolution almost remains similar to the first interaction except more wrinkles are formed along the flame front. The repeated interactions between the flame and pressure waves result in the oscillations of the flame tip position and the flame speed, as clearly shown in Figs. 5 and 6, respectively. Note that the negative flame speed corresponds to the decrease of the flame tip position as the flame front is pushed back by the pressure wave at the first stage during each interaction as discussed above. The detailed mechanism of flame-pressure wave interactions will be discussed in Sec. III B.

Due to the repeated reflections of the pressure waves at the right end wall, the temperature and reactivity of the end-gas near the right wall both increase, resulting in the autoignition at about 175 μs. As shown in Fig. 6, the autoignition front (AIF) propagates to the left at the speed of about 1900 m/s and develops into an overdriven detonation, which will be clearly observed later, with the speed of about 2300 m/s exceeding the local Chapman-Jouguet (CJ) detonation speed of 1984 m/s for the mixture at a temperature of about 1230 K and pressure of 29 atm. Then, at the position of 1.7 cm, the detonation wave meets the normal flame front and starts to decelerate. This is because the fresh mixture has been consumed completely by the normal flame and no chemical reaction can provide energy to the detonation wave.

B. Pressure wave propagation and the mechanism of flame-pressure wave interactions

The normal flame ignited by the hot kernel and autoignition in the end-gas region are separated in space but connected by pressure waves; thus, the pressure wave generation and its propagation in the closed chamber play a crucial role in the process. The numerical schlieren images in Fig. 8 clearly show the process

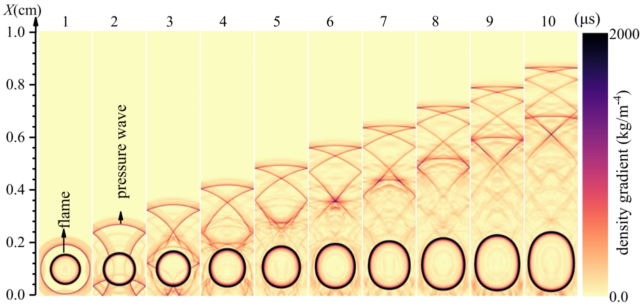

FIG. 8. Sequence of numerical schlieren images during the process of pressure wave generation by the flame acceleration at early time.

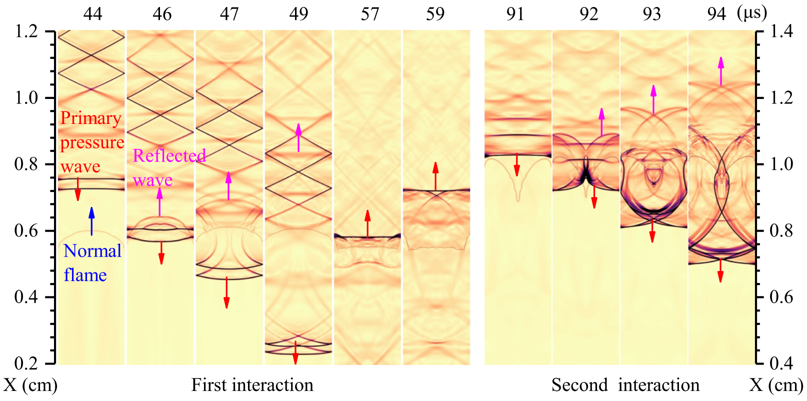

FIG. 9. Sequence of numerical schlieren images during the processes of the first and second flame-pressure wave interactions. The red, blue, and magenta arrows denote the propagation direction of primary pressure wave, normal flame, and reflected wave, respectively.

of pressure wave generation by the flame acceleration at early time. As mentioned above, the flame front accelerates exponentially after ignition and resembles an accelerating piston that compresses the unburned mixture ahead of it, resulting in the generation of a series of pressure waves. Because of consecutive multiple pressure wave generations and reflections in the confined chamber, many crossed structures are produced successively along the centerline, as shown in Fig. 8. According to the thermodynamics, the temperature behind the pressure wave is increased by compression, and thus the pressure waves in the back propagate faster than in the front; thus, the former will catch up with the latter and coalesce with them. This can be determined by the leading pressure wave (LPW) propagation from 6 μs to 10 μs. With the superposition of the pressure waves, the intensity of the leading pressure wave is enhanced continually and is consequently strong enough to dominate its interactions with the flame, which is recognized as a primary pressure wave (PPW) in the present work. However, the pressure waves are generated all the time during flame propagation, and some pressure waves may not catch up with the leading pressure wave and coalesce with it, which are called secondary pressure waves here. It should be noted that although the secondary pressure waves have only marginal effects on the process of flame-pressure wave interactions owing to their relatively weaker intensities, they can significantly influence the autoignition occurrence which is extremely sensitive to the thermodynamics state, as discussed later. The pressure wave configurations during the first and second flame-pressure wave interactions can be clearly uncovered in Fig. 9 with numerical schlieren images. It is noted that the shapes of pressure waves after interactions extremely resemble that of the flame front. As can be seen, when the pressure waves meet the normal flame at the first time, the bow-shaped flame front results in the same shape of the transmitted and reflected pressure waves (RPW2), while they show a structure of two crossed bows at the second interaction because of the tulip flame front.

There is no doubt that a wave diagram is a good choice to help us in obtaining a more comprehensive understanding of the overall process of the flame-pressure wave interactions in the confined chamber. Figure 10 shows the wave diagram constructed from the numerical schlieren images, where the normal flame front, pressure waves, and detonation wave can all be observed. The dotted arrows are added for more explicit observation of the primary pressure wave. It should be noted that the points in the diagram are selected along the centerline; thus, the profile of the flame front position is different from that in Fig. 5. As can be seen, with the flame acceleration, multiple pressure waves are generated from the flame front and coalesce continually during propagation as discussed above. The primary pressure wave propagates to the left (downwards in Fig. 10) after being reflected at the right wall and interacts with the flame front, sequentially producing the reflected waves propagating reversely. Note that the "thickened" flame front at about 85, 130, and 170 μs is caused by the meeting at the centerline of two cusps, which produces a reverse cusp at the centerline as can be seen in Fig. 7. Meanwhile, the collapse of the reverse cusp at the centerline results in the acceleration of the flame position, as shown in Fig. 10. In addition, the period and the speed of the pressure wave propagation can be evaluated from the diagram. According to the thermal dynamics, the pressure wave propagation speed is faster for a higher temperature, which can be clearly identified by the steeper slope of the line in the burned mixture. With the flame propagation, the region with a high temperature is enlarged increasingly, resulting in the increase in the average pressure wave speed from about 800 m/s to

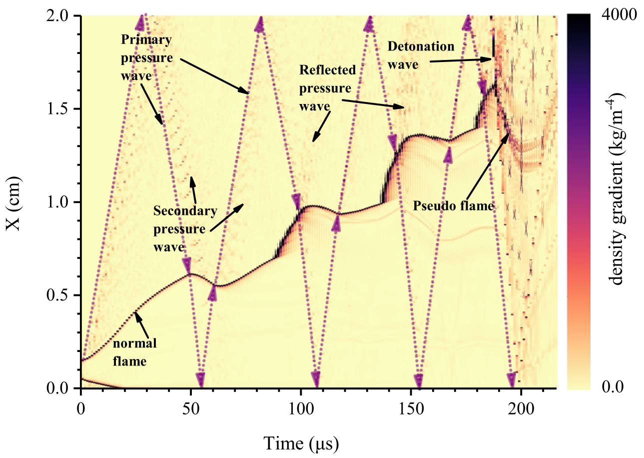

FIG. 10. Wave diagram.

1000 m/s as well as the decrease in the period from about 50 μs to 40 μs. Another interesting phenomenon, not clearly observed in other images, is displayed from the wave diagram that the "pseudo flame front" is pushed back much further by the detonation wave compared to the flame-pressure wave interactions. It is called "pseudo flame front" because a real flame front cannot exist as a result of complete consumption of the fresh mixture by the detonation development.

To further investigate the mechanism of tulip flame formation during interactions in the confined space, Fig. 11 shows the temporal evolution of flow velocity and pressure field around the flame front during the first flame-pressure interaction. As can be seen at 44 μs, the flow velocity ahead of the flame front is horizontally toward the right as a result of the expansion of combustion product before being influenced by the pressure wave propagating to the left. Then, it is continually reduced and even turns to the left after the primary and secondary pressure waves pass through the field successively, which results in the deceleration and backward propagation of the flame front as shown from 46 μs to 52 μs. Meanwhile, two reverse cusps appear near the sidewalls, owing to the effect of the boundary layer. In order to have a deep understanding of the phenomenon, Fig. 12 shows the profiles of flame front and velocity u at cross sections A, B, and C corresponding to Fig. 11. Here, the boundary layer is defined as the field whose velocity u at section A is less than 0.99 of its maximum. Note that the profile of velocity u is monotonously decreasing from the centerline to the wall in the boundary layer at section A, while they show the trend of increase first and then decrease at both sections B and C. Actually, after the pressure waves are produced by the flame acceleration, propagate to the right, and pass through the field ahead of the flame front at the first time, the positive velocity u distributed like that at section A is formed because of the viscous effect and no-slip wall, as discussed in Refs. 46 and 49. Then, the pressure waves are reflected at the right wall, propagate to the left, and pass through the field once more, whose disturbance on the flow velocity will be added into the existing distribution of that. If one only considers the velocity distribution induced by the pressure wave propagating to the left without the effect of no-slip wall, it should be negative and uniform along the section. Therefore, when this negative and uniform distribution is added into the profile of velocity u with a decreasing trend in the boundary layer as shown at section A, the field with smaller positive velocity u can obtain bigger negative velocity u, which produces the increasing trend from the centerline to the region near the wall. On the other hand, the velocity u at the wall should keep zero as a result of the no-slip condition, which produces the decreased trend in the field close to the wall. A similar trend of the velocity is also observed in Ref. 24, but a further explanation is not given there. It should be noted that the position of the reverse cusp of the flame front is nearly the same as that of the turning point of velocity u in the boundary layer, which indicates that the propagation of the flame front is mainly dominated by the flow velocity ahead of it. The flame front close to the wall can keep stationary, thanks to the smaller flow velocity, while the rest part of it is pushed backwards owing to the bigger negative flow velocity ahead of it. Because of these two opposite constraints, the flame front near the wall is stretched continually as shown from 52 μs to 56 μs, increasing the flame surface area and the heat release rate. The oblique stretched flame sequentially makes the flow velocity ahead of it rotate a small degree anticlockwise, and this rotation is further enhanced by the primary pressure wave propagating to

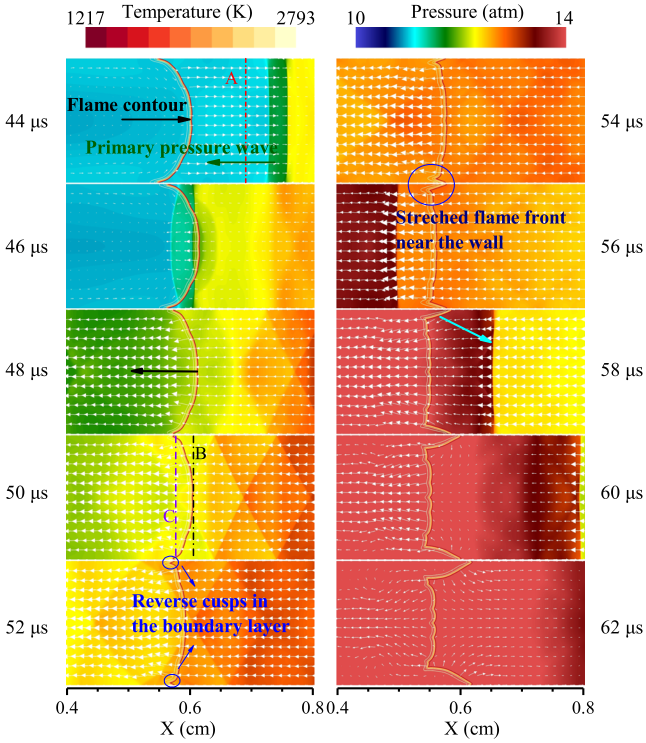

FIG. 11. Temporal evolutions of flow velocity and pressure field around the flame front during the first flame-pressure interaction. The flame front is identified by the isothermal lines of 1200 K–2700 K. The black and green arrows denote the propagation direction of the normal flame and primary pressure wave, respectively. Section A is located between the flame front and the primary pressure wave. Section B is located at the front of the flame tip. Section C is located at the front of the flame front at the boundary layer.

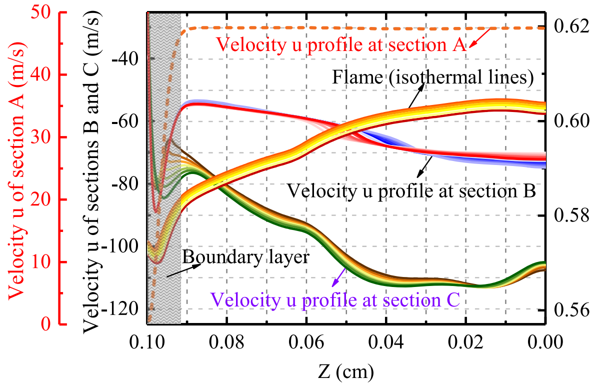

FIG. 12. Profiles of the flame front and velocity u at the cross sections A, B, and C corresponding to Fig. 11. Only upper half part is shown. The minus means the velocity direction is toward the left. Note that the velocity u at multiple sections closely ahead of sections B and C is also added for better observation of trend. The flame front is identified by multiple isothermal lines.

the right. Consequently, the velocity turns to the centerline and the right, increasingly accelerating and amplifying the stretched flame near the walls in turn, which results in the formation of the tulip flame finally. A great many mechanisms in the previous works[23,64–67] have been presented that can lead to the formation of the tulip flame, such as the Taylor instability,[23] effect of vortex in the burned gas,[65,67] and Darrieus–Landau instability.[64] In addition, the "distorted tulip" flame, induced by the Rayleigh–Taylor instability regarding flame-pressure wave interactions, is comprehensively investigated by Xiao *et al.*[24–26] as mentioned early. However, different from the works cited above, the evolution of the tulip flame dominated by a combined effect of the viscous boundary layer and pressure waves may be found in the present study for the first time. Furthermore, it should be noted that the adiabatic walls are applied here so that the flame can exist in the fields close to the walls, while the flame evolution may be distinct with the isothermal walls where a thermal boundary layer can exist.[49] On the other hand, the flame acceleration rate can be reduced because of the heat losses,[68] which can further weaken the strength of pressure waves compared to adiabatic condition and consequently influence the process of flame-pressure wave interactions.

C. Autoignition and detonation development in the end gas

Owing to the multiple reflections of the primary pressure wave at the right wall, the temperature and reactivity of the end gas are increased gradually, which provides a favorable condition for occurrence of autoignition. The profiles of temperature and pressure along the centerline during autoignition and detonation development are demonstrated in Fig. 13. As can be seen, the autoignition takes place at the right end wall at about 175 μs, and before that, the temperature of the end gas increases from 1000 K to around 1230 K. Then, the autoignition front propagates to the left and subsequently develops into a detonation wave with a steep increase in temperature and pressure. Because of the detonation development, the peak pressure reaches up to over 200 atm, which is equivalent to that of the superknock condition in engines. After the detonation wave meets the normal flame front, its intensity decreases and the peak pressure is reduced to 70 atm because the fresh mixture ahead of it has been completely consumed by the normal flame and no heat release can support the detonation.

Figure 14 shows the process of detonation development induced by the autoignition. For clear observation, the images are composed by the pressure gradient at the left half and the temperature contour at the right half. As can be seen, the autoignition zone completely covers the end wall and near the corner regions at 175 μs, meanwhile local detonation kernels identified by the high pressure gradient appear near the corners, ahead of which two leading pressure waves are clearly captured as well close to the sidewalls. Note that the leading pressure wave here is different from that mentioned above in Fig. 8. With the leading pressure wave propagation, the preheat zones are formed behind of them, which results in the spread of autoignition along the sidewalls. At the same time, the detonation kernels expand, propagating with the autoignition front formed near the end all side by side, and consequently, they develop into a detonation wave of concave shape at 175.4 μs. In addition, the cellular structure at the detonation wave front is observed as shown in Fig. 15, but it is not able to further develop because of its meeting with the normal flame. As a result of the absence of fresh mixture, the detonation wave degenerates to a shock wave as interacting with the normal flame. Also, due to the hydrodynamic instability, vortices are generated after the interaction of the shock wave and flame front at 177 μs.

However, it is curious that the detonation kernels are formed near the corner regions at first. To figure out the underlying reason, Fig. 16 shows the temporal evolutions of OH mass fractions, temperatures, and ignition delay times at specific four points, including (X = 2, Z = 0), (X = 1.95, Z = 0), (X = 2, Z = 0.1), (X = 1.95, Z = 0.1), which can represent the regions at the end wall and near the wall, and at the corner and near the corner, respectively. Note that the ignition delay time is evaluated by the Closed

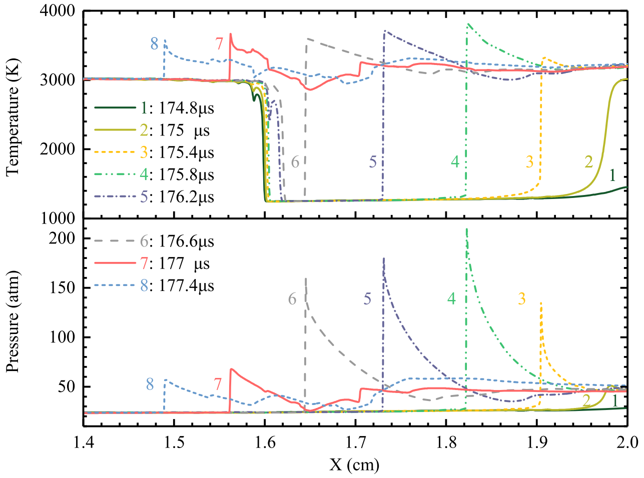

FIG. 13. Profiles of temperature and pressure along the centerline during autoignition and detonation initiation.

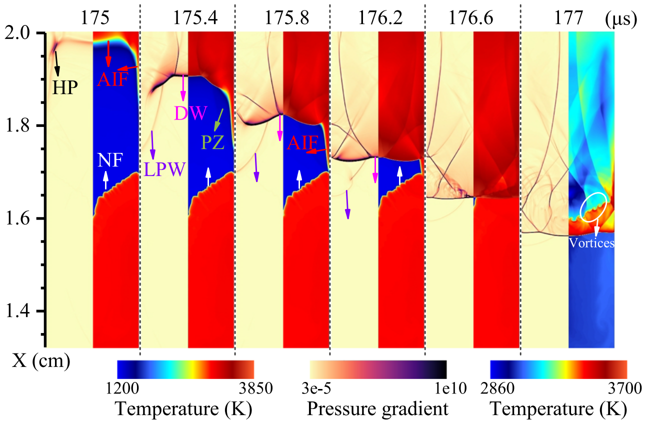

FIG. 14. Sequence of images composed by pressure gradient (left) and temperature contour (right) during detonation development. HP-high pressure, AIF-autoignition front, NF-normal flame, LPW-leading pressure wave, DW-detonation wave, and PZ-preheat zone. The corresponding arrows indicate their propagation directions.

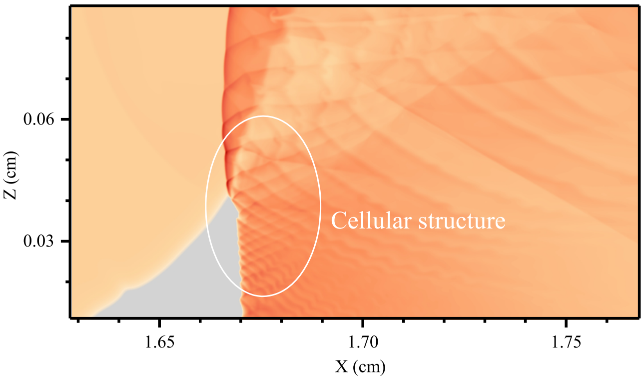

FIG. 15. Cellular structure of the detonation wave.

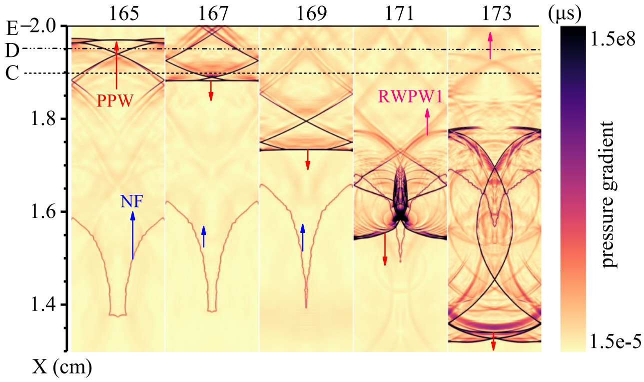

FIG. 17. Sequence of numerical schlieren images of pressure wave propagation at the earlier stage before autoignition. The red, blue, and magenta arrows denote the propagation direction of the primary pressure wave, normal flame, and reflected wave, respectively. RWPW1-reflected weak pressure wave1. Sections C, D, and E are located at x = 1.90, 1.95, and 2.0 cm, respectively.

Homogeneous model in Chemkin PRO[47] with local temperature, pressure, and species mass fractions at each time and point as initial input parameters. The OH mass fractions selected here can identify the reactivity of these regions. It is indicated that there are oscillations in the temporal evolutions of OH mass fractions as well as temperatures, but the average values are all increased gradually with the primary pressure wave propagation, which consequently reduces ignition delay times at these regions. After the fourth reflection of the primary pressure wave at about 165 μs, the ignition delay times all reduce to less than 10 μs, and sequentially, the temperatures do not decrease like first three reflections but increase gradually, which causes the rapid decrease in the ignition delay times and eventually autoignition occurrence. It means that the critical thermodynamics state has been reached after the fourth reflection of the primary pressure wave so that any small disturbance is possible to result in autoignition occurrence. However, the time of detonation initiation at these regions cannot be identified clearly from this figure.

To further investigate the mechanism in detail, the numerical schlieren images of pressure wave propagation from 165 μs to 174.8 μs are described in Figs. 17 and 18, which covers the fourth reflection of the primary pressure wave at the right end wall and other weak pressure wave propagation before autoignition. Meanwhile, the temperature profiles of three cross sections C, D, and E, at X = 1.9, 1.95, 2.0 cm, respectively, are selected to identify the influence of pressure wave propagation on temperature distributions in the end gas, as shown in Figs. 19 and 20. It is seen that the crossed structures are developed because of multiple consecutive pressure wave reflections at the sidewalls, as discussed above, which results in the nonuniform distribution of temperature at these cross sections. The temperature in different regions at the same cross section is increased by turns as the crossed structures pass through them, and there is not any fixed temperature difference among these regions at all three sections before 173 μs, as shown in Fig. 19. However, the situation changes later. A reflected weak pressure wave (RWPW1) is produced when the primary pressure wave meets the flame front, and it propagates toward the right end wall at 171 μs, as shown

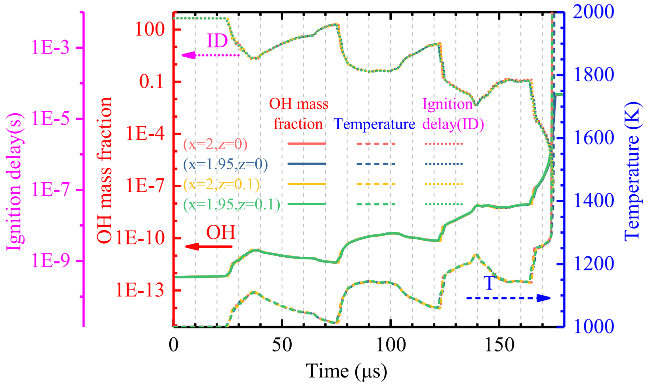

FIG. 16. Temporal evolutions of ignition delay times, OH mass fractions, and temperatures at four points in the end-gas region.

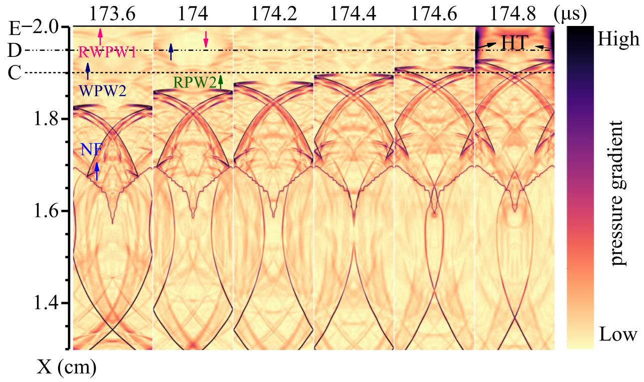

FIG. 18. Sequence of numerical schlieren images of pressure wave propagation at the later stage before autoignition. The red arrow denotes the propagation direction of the normal flame, and the other arrows denote the direction of pressure waves. WPW2-weak pressure wave2, RPW2-reflected pressure wave2, and HT-high temperature.

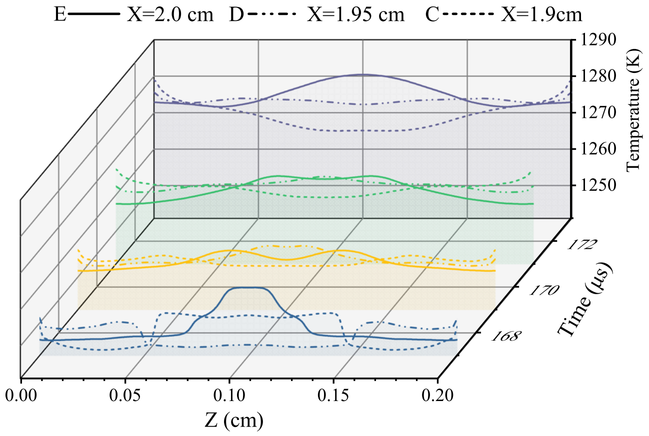

FIG. 19. Temporal evolution of temperature profiles at cross sections C, D, and E in Fig. 17.

in Fig. 17. Then, RWPW1 reaches the right end wall at about 173.6 μs, as shown in Fig. 18, when the concave temperature distributions appear at the cross sections, which means the temperature at the sidewalls is slightly higher than that near the centerline. After being reflected at the right end wall, RWPW1 propagates to the left and meets another weak pressure wave (WPW2) at 174 μs. After that, the difference between the temperature at the sidewalls and near the centerline is amplified continually, and consequently, the obvious high temperature zones appear at the sidewalls near the corners at 174.8 μs. It should be noted that there is another stronger reflected pressure wave (RPW2) produced by the flame-pressure wave interaction, but autoignition takes place before its arrival. Thus, it is the earlier autoignition occurrence near the corner region that leads to the detonation initiation at first there.

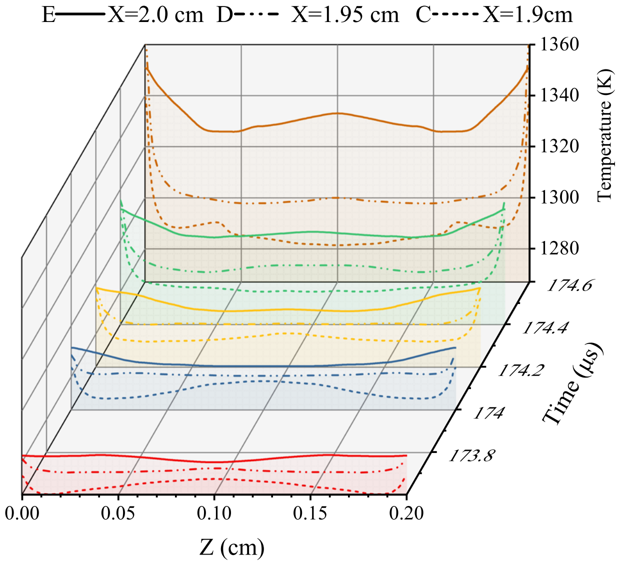

FIG. 20. Temporal evolution of temperature profiles at cross sections C, D, and E in Fig. 18.

As a consequence, the higher temperature at the sidewalls than the other region is the conclusive reason for the order of autoignition occurrence as well as detonation initiation in the present work. Based on the above observation, there exist two possible causes for this temperature difference. On the one hand, the 1D simulations conducted by Terashima *et al.*[42] demonstrated that the wall reflections periodic of the compression waves produce a larger temperature increase at the wall compared to other end-gas points, which further leads to the production of a larger amount of chemical species. Similarly, because of the presence of the crossed-structure, the pressure waves in the present work not only reflect at the end walls but also reflect at the sidewalls, which can lead to a larger temperature increase at the sidewalls. But there is no doubt that this temperature increase is much less than that induced by the reflections of primary pressure wave at the end walls. On the other hand, as shown in Fig. 18, both RWPW1 and WPW2 are concave so that the side wall is compressed at first all the time during the pressure wave propagation. As mentioned above, after the fourth reflection of the primary pressure wave, the thermodynamics state of the end gas has been promoted to a critical level, and the small difference of compression time caused by the pressure wave shape is extremely possible to earlier improve the reactivity dramatically at the sidewalls and to further accelerate local heat release, which consequently results in the earlier occurrence of autoignition at the sidewalls. Note that the nonuniform temperature distribution is totally caused by the pressure wave structures here, while in the real engine condition, it can also be induced by the heat losses and turbulence that are both negligible in the present work, which can lead to the uncertainty of the position and time of autoignition occurrence.[42,43,69–72] Specifically, heat losses to the walls often make autoignition occur apart from the walls rather than at the walls like in the current study.[42,72] As for turbulence, by affecting temperature and species distributions, turbulent mixing can change the reactivity gradient inside the hot kernel and thus can delay autoignition/detonation transition and dramatically reduce detonation strength.[43,73,74] In addition, by increasing the flame speed, turbulence can change the competition between flame propagation and autoignition. Chen *et al.*[75] found that the faster flame propagation with increased turbulence intensity can facilitate autoignition under lower turbulence intensity and further increased turbulence intensity can suppress knocking combustion. However, more detailed effects of turbulence and hot losses need to be further investigated in the future.

IV. CONCLUSIONS

In this work, the entire process of flame-pressure wave interactions with end-gas autoignition and detonation development in a confined chamber is comprehensively investigated by 2D numerical simulations with a reduced chemical kinetics mechanism of H_2. Six stages, including a spherical flame, a finger flame, a flame with its skirt touching the sidewalls, flame-pressure wave interactions, autoignition induced by flame-wave interactions, and detonation development, are distinguished in the overall process for the flame propagation in the confined space. The simulations suggest that the violent oscillations of the flame shape and speed are induced by the flame-pressure wave multi-interactions in the confined chamber. Three stages of the flame shape evolution during each flame-pressure wave interaction are observed in the present work, which includes backward propagation of the flame front, stretch of the flame front at the boundary layer, and formation of the tulip flame. The results show that the combined effects of the viscous boundary layer and pressure waves, where the former makes the flame front keep stationary and the latter pushes the flame back, determine the formation of the tulip flame.

The crossed structures are observed because of consecutive multiple pressure wave generations by the flame acceleration and reflections at the sidewalls. It is indicated that the leading pressure wave is strengthened by the superposition with the pressure waves behind it and dominates the flame-pressure wave interactions, while the weak pressure waves that do not catch up with the leading pressure wave have only marginal effects on the interactions, but they can significantly influence the autoignition occurrence. It is also found that shapes of pressure waves after interactions with the flame front extremely resemble that of the flame front. In addition, the results show that the velocity distributions in the boundary layer show the trend of increase first and then decrease after the pressure waves pass the fields twice in the opposite directions. The wave diagram, including the flame front, primary pressure wave, secondary pressure waves, reflected waves, transmitted waves, and detonation wave, provides an integral understanding of the pressure wave propagation and flame-pressure wave interactions in the confined chamber.

The temperature and reactivity of the end gas are increased by the multiple reflections of the primary pressure wave at the right wall, which leads to the decrease in the local ignition delay time. It is shown that the thermodynamics state of the end gas has been promoted to a critical level after the fourth reflection of the primary pressure wave and is extremely sensitive to even small disturbances. As a result, the autoignition and detonation initiation occur near the corners at first and then take place at the right end wall because of the slightly nonuniform temperature distributions induced by the specific pressure wave structures.

ACKNOWLEDGMENTS

The work was supported by The Key Program of the National Natural Science Foundation of China (Grant No. 91641203) and National Natural Science Foundation of China (Grant No. 91741119). This paper was supported by the opening project of State Key Laboratory of Explosion Science and Technology (Beijing Institute of Technology), the opening Project No. KFJJ18-09M. Special thanks to Dr. Xiaodong Cai at the National University of Defense Technology for his guidance and help in the numerical codes.

APPENDIX: DISCUSSIONS ON NUMERICAL SIMULATION

1. Effects of initial temperature and pressure on autoignition and detonation development

Simulations with different initial temperatures and pressures are conducted to investigate their effects on the process of autoignition and detonation development. Figure 21 shows the temporal histories of the temperatures and pressures at the point (x = 2, z = 0) under different initial conditions. It should be noted that autoignition does not take place at T_0 = 900 K, and the case acts as a reference. The results show that compared to the initial pressure, the initial temperature has a predominant influence on the autoignition time. The higher the initial temperature is, the earlier the autoignition occurs. It can be clearly identified that the maximum amplitudes of the pressure oscillations are larger in the cases with autoignition and detonation development, which is consistent with knock occurrence in engines.

2. Effects of dimensions on flame-pressure interactions and detonation development

A simulation with the same boundary conditions and aspect ratio but larger dimensions of l = 8 cm and d = 0.8 cm is also conducted. As shown in Fig. 22, the entire process of flame-pressure wave interactions and especially the formation of the tulip flame are qualitatively similar to that in smaller dimensions. However, except detonation development at the end wall, spherical detonation waves (SDWs) initiated by autoignition ahead of the flame front are also observed in the lager dimensions, as shown in Fig. 23.

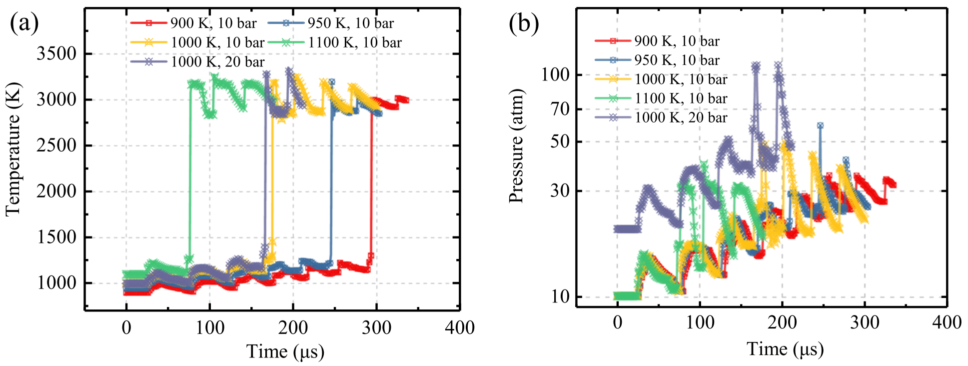

FIG. 21. Temporal histories of the temperatures (a) and pressures (b) at the point (x = 2, z = 0) under different initial conditions.

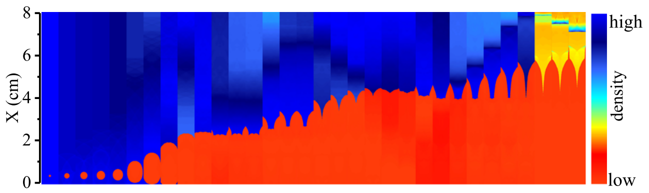

FIG. 22. Entire process of flame propagation and detonation development with dimensions of l = 8 cm and d = 0.8 cm.

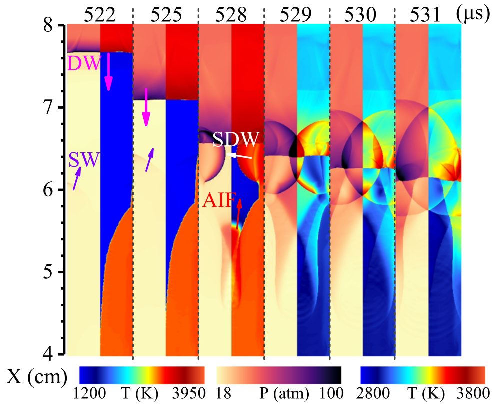

FIG. 23. Sequence of images composed by pressure (left) and temperature contour (right) during detonation development with dimensions of l = 8 cm and d = 0.8 cm. AIF-autoignition front, NF-normal flame, SW-shock wave, DW-detonation wave, and SDW-spherical detonation wave. The corresponding arrows indicate their propagation directions.

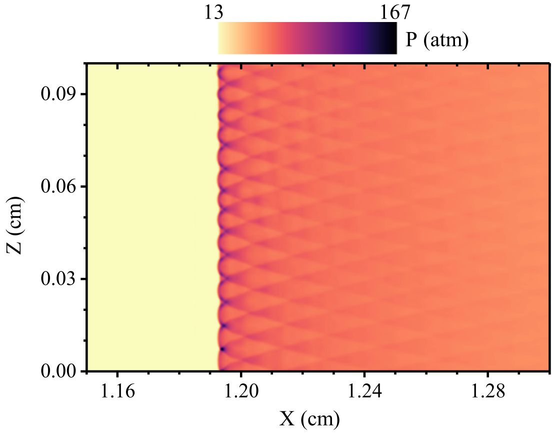

FIG. 25. Detonation cellular structure at T_0 = 1100 K, P_0 = 10 bars.

The collision of these detonation waves results in a stronger peak pressure in the channel. But the detailed process of the autoignition and detonation development is not analyzed here, and we mainly discuss the possible causes responsible for this difference. As mentioned above, the thermodynamics state of the end gas has been promoted to a critical level before autoignition and is extremely sensitive to even small disturbances. With larger dimensions, many factors, including the moments of flame-pressure wave interactions, intensity of pressure waves, flame shape, pressure wave structures in the end gas, and so on, can be different from the smaller dimensions and have an influence on the reactivity of end gas before autoignition, which further results in different autoignition modes here. Actually, knocking combustion under real engine conditions often has different intensities,[12,15,44] which can correspond to different autoignition modes such as autoignition without detonation, developing detonation, collision of multiple detonation waves, and so on. This uncertainty can be induced by turbulence, inhomogeneity, as well as dimensions here.[40,73–75] However, pressure wave propagation and reflection as discussed in the present work can play an important role in all these modes.

3. Grid resolution

To further validate the grid resolution, Fig. 24 shows 1D flame internal structure at the centerline extracted from 2D data at 34 μs. As can be seen, the distributions of temperature and species mass fractions along the flame front can all be reasonably resolved under current resolution. In addition, a case with T_0 = 1100 K is also conducted as discussed in Subsection 1 of the Appendix, where the earlier autoignition provides enough unburned mixture for detonation development; thus, the regular cellular structure is clearly captured, as shown in Fig. 25. Therefore, the present resolution may not be able to resolve the finest structure of the detonation wave; however, it can give a fully reasonable description of the phenomenon focused in the present work.

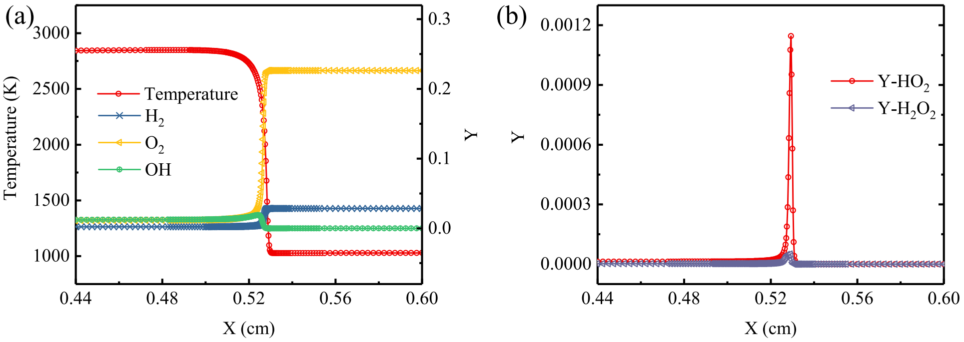

FIG. 24. Flame structure at the centerline at 34 μs. (a) Profiles of temperature and mass fractions of species H_2, O_2, OH. (b) Profiles of mass fractions of species HO_2 and H_2O_2.

REFERENCES

[1] V. Akkerman and D. Valiev, "Moderation of flame acceleration in obstructed cylindrical pipes due to gas compression," Phys. Fluids **30**, 106101 (2018).

[2] K. Bioche, L. Vervisch, and G. Ribert, "Premixed flame–wall interaction in a narrow channel: Impact of wall thermal conductivity and heat losses," J. Fluid Mech. **856**, 5 (2018).

[3] V. N. Gamezo, T. Ogawa, and E. S. Oran, "Flame acceleration and DDT in channels with obstacles: Effect of obstacle spacing," Combust. Flame **155**, 302 (2008).

[4] A. Chinnayya, A. Hadjadj, and D. Ngomo, "Computational study of detonation wave propagation in narrow channels," Phys. Fluids **25**, 036101 (2013).

[5] W. Han, Y. Gao, C. Wang, and C. K. Law, "Coupled pulsating and cellular structure in the propagation of globally planar detonations in free space," Phys. Fluids **27**, 106101 (2015).

[6] M.-h. Wu, M. P. Burke, S. F. Son, and R. A. Yetter, "Flame acceleration and the transition to detonation of stoichiometric ethylene/oxygen in microscale tubes," Proc. Combust. Inst. **31**, 2429 (2007).

[7] M. Reynaud, F. Virot, and A. Chinnayya, "A computational study of the interaction of gaseous detonations with a compressible layer," Phys. Fluids **29**, 056101 (2017).

[8] M. A. Liberman, M. Kuznetsov, A. Ivanov, and I. Matsukov, "Formation of the preheated zone ahead of a propagating flame and the mechanism underlying the deflagration-to-detonation transition," Phys. Lett. A **373**, 501 (2009).

[9] M. A. Liberman, M. F. Ivanov, A. D. Kiverin, M. S. Kuznetsov, A. A. Chukalovsky, and T. V. Rakhimova, "Deflagration-to-detonation transition in highly reactive combustible mixtures," Acta Astronaut. **67**, 688 (2010).

[10] Y. Qi, Z. Wang, J. Wang, and X. He, "Effects of thermodynamic conditions on the end gas combustion mode associated with engine knock," Combust. Flame **162**, 4119 (2015).

[11] J. Rudloff, J. M. Zaccardi, S. Richard, and J. M. Anderlohr, "Analysis of pre-ignition in highly charged SI engines: Emphasis on the auto-ignition mode," Proc. Combust. Inst. **34**, 2959 (2013).

[12] A. Robert, S. Richard, O. Colin, and T. Poinsot, "LES study of deflagration to detonation mechanisms in a downsized spark ignition engine," Combust. Flame **162**, 2788 (2015).

[13] H. Wei, D. Gao, L. Zhou, D. Feng, and R. Chen, "Different combustion modes caused by flame-shock interactions in a confined chamber with a perforated plate," Combust. Flame **178**, 277 (2017).

[14] H. Wei, J. Zhao, L. Zhou, D. Gao, and Z. Xu, "Effects of the equivalence ratio on turbulent flame–shock interactions in a confined space," Combust. Flame **186**, 247 (2017).

[15] Z. Wang, H. Liu, and R. D. Reitz, "Knocking combustion in spark-ignition engines," Prog. Energy Combust. Sci. **61**, 78 (2017).

[16] G. H. Markstein, "A shock-tube study of flame front-pressure wave interaction," Symp. (Int.) Combust. **6**, 387 (1956).

[17] G. Searby, "Acoustic instability in premixed flames," Combust. Sci. Technol. **81**, 221 (1992).

[18] V. Bychkov, "Analytical scalings for flame interaction with sound waves," Phys. Fluids **11**, 3168 (1999).

[19] V. Bychkov, "Stabilization of the hydrodynamic flame instability by a weak shock," Phys. Fluids **10**, 2669 (1998).

[20] A. Petchenko, V. Bychkov, V. Akkerman, and L. Eriksson, "Flame–sound interaction in tubes with nonslip walls," Combust. Flame **149**, 418 (2007).

[21] A. Petchenko, V. Bychkov, V. Akkerman, and L. E. Eriksson, "Violent folding of a flame front in a flame-acoustic resonance," Phys. Rev. Lett. **97**, 164501 (2006).

[22] V. Akkerman and C. K. Law, "Effect of acoustic coupling on power-law flame acceleration in spherical confinement," Phys. Fluids **25**, 013602 (2013).

[23] G. S. C. Clanet, "On the 'tulip flame' phenomenon," Combust. Flame **105**, 225 (1996).

[24] H. Xiao, R. W. Houim, and E. S. Oran, "Formation and evolution of distorted tulip flames," Combust. Flame **162**, 4084 (2015).

[25] H. Xiao, R. W. Houim, and E. S. Oran, "Effects of pressure waves on the stability of flames propagating in tubes," Proc. Combust. Inst. **36**, 1577 (2017).

[26] H. Xiao, D. Makarov, J. Sun, and V. Molkov, "Experimental and numerical investigation of premixed flame propagation with distorted tulip shape in a closed duct," Combust. Flame **159**, 1523 (2012).

[27] G. Thomas, R. Bambrey, and C. Brown, "Experimental observations of flame acceleration and transition to detonation following shock-flame interaction," Combust. Theory Modell. **5**, 573 (2001).

[28] Y.-J. Zhu, G. Dong, Y.-X. Liu, B.-C. Fan, and H. Jiang, "Effect of chemical reactivity on the detonation initiation in shock accelerated flow in a confined space," Acta Mech. Sin. **29**, 54 (2013).

[29] Y. Zhu, G. Dong, and Y. Liu, "Three-dimensional numerical simulations of spherical flame evolutions in shock and reshock accelerated flows," Combust. Sci. Technol. **185**, 1415 (2013).

[30] H. H. Teng, Z. L. Jiang, and Z. M. Hu, "Detonation initiation developing from the Richtmyer–Meshkov instability," Acta Mech. Sin. **23**, 343 (2007).

[31] Y. B. Zeldovich, "Regime classification of an exothermic reaction with nonuniform initial conditions," Combust. Flame **39**, 211 (1980).

[32] L. Bates, D. Bradley, G. Paczko, and N. Peters, "Engine hot spots: Modes of auto-ignition and reaction propagation," Combust. Flame **166**, 80 (2016).

[33] D. Bradley and G. T. Kalghatgi, "Influence of autoignition delay time characteristics of different fuels on pressure waves and knock in reciprocating engines," Combust. Flame **156**, 2307 (2009).

[34] X. J. Gu, D. R. Emerson, and D. Bradley, "Modes of reaction front propagation from hot spots," Combust. Flame **133**, 63 (2003).

[35] Z. Wang, Y. Qi, X. He, J. Wang, S. Shuai, and C. K. Law, "Analysis of pre-ignition to super-knock: Hotspot-induced deflagration to detonation," Fuel **144**, 222 (2015).

[36] Z. Wang, Y. Qi, H. Liu, P. Zhang, X. He, and J. Wang, "Shock wave reflection induced detonation (SWRID) under high pressure and temperature condition in closed cylinder," Shock Waves **26**, 687 (2016).

[37] D. G. H. Wei, L. Zhou, J. Pan, K. Tao, and Z. Pei, "Experimental observations of turbulent flame propagation effected by flame acceleration in the end gas of closed combustion chamber," Fuel **180**, 157 (2016).

[38] P. Dai and Z. Chen, "Supersonic reaction front propagation initiated by a hot spot in *n*-heptane/air mixture with multistage ignition," Combust. Flame **162**, 4183 (2015).

[39] M. A. Liberman, M. F. Ivanov, O. E. Peil, D. M. Valiev, and L. E. Eriksson, "Numerical modeling of the propagating flame and knock occurrence in spark-ignition engines," Combust. Sci. Technol. **177**, 151 (2004).

[40] C. Qi, P. Dai, H. Yu, and Z. Chen, "Different modes of reaction front propagation in *n*-heptane/air mixture with concentration non-uniformity," Proc. Combust. Inst. **36**, 3633 (2017).

[41] H. Terashima and M. Koshi, "Mechanisms of strong pressure wave generation in end-gas autoignition during knocking combustion," Combust. Flame **162**, 1944 (2015).

[42] H. Terashima, A. Matsugi, and M. Koshi, "Origin and reactivity of hot-spots in end-gas autoignition with effects of negative temperature coefficients: Relevance to pressure wave developments," Combust. Flame **184**, 324 (2017).

[43] H. Wei, C. Chen, H. Zhou, W. Zhao, and Z. Ren, "Effect of turbulent mixing on the end gas auto-ignition of *n*-heptane/air mixtures under IC engine-relevant conditions," Combust. Flame **174**, 25 (2016).

[44] H. Yu and Z. Chen, "End-gas autoignition and detonation development in a closed chamber," Combust. Flame **162**, 4102 (2015).

[45] W. Han, Y. Gao, and C. K. Law, "Flame acceleration and deflagration-to-detonation transition in micro-and macro-channels: An integrated mechanistic study," Combust. Flame **176**, 285 (2017).

[46] V. N. Gamezo and E. S. Oran, "Flame acceleration in narrow channels: Applications for micropropulsion in low-gravity environments," AIAA J. **44**, 329 (2006).

[47] CHEMKIN-PRO 10131, Reaction Design, San Diego, 2013.

[48] J. Li, Z. Zhao, A. Kazakov, and F. L. Dryer, "An updated comprehensive kinetic model of hydrogen combustion," Int. J. Chem. Kinet. **36**, 566 (2004).

[49] J. D. Ott, E. S. Oran, and J. D. Anderson, "A mechanism for flame acceleration in narrow tubes," AIAA J. **41**, 1391 (2003).

[50] J. Daou and M. Matalon, "Influence of conductive heat-losses on the propagation of premixed flames in channels," Combust. Flame **128**, 321 (2002).

[51] L. Kagan and G. Sivashinsky, "On the transition from deflagration to detonation in narrow tubes," Flow, Turbul. Combust. **84**, 423 (2010).

[52] R. Kee, F. Rupley, and J. Miller, "CHEMKIN-II: A Fortran chemical kinetics package for the analysis of gas-phase chemical kinetics," Document No. SAND-89-8009, 1989.

[53] R. Deiterding, "High-resolution numerical simulation and analysis of Mach reflection structures in detonation waves in low-pressure H_2–O_2–Ar mixtures: A summary of results obtained with the adaptive mesh refinement framework AMROC," J. Combust. **2011**, 1.

[54] R. Deiterding, "A parallel adaptive method for simulating shock-induced combustion with detailed chemical kinetics in complex domains," Comput. Struct. **87**, 769 (2009).

[55] R. Deiterding, "Parallel adaptive simulation of multi-dimensional detonation structures," Ph.D. dissertation (Brandenburgische Technische Universität Cottbus, 2003).

[56] J. L. Ziegler, R. Deiterding, J. E. Shepherd, and D. I. Pullin, "An adaptive high-order hybrid scheme for compressive, viscous flows with detailed chemistry," J. Comput. Phys. **230**, 7598 (2011).

[57] P. N. Brown, G. D. Byrne, and A. C. Hindmarsh, "VODE: A Variable coefficient ODE solver," SIAM J. Sci. Stat. Comput. **10**, 1038 (1989).

[58] X. Cai, R. Deiterding, J. Liang, and Y. Mahmoudi, "Adaptive simulations of viscous detonations initiated by a hot jet using a high-order hybrid WENO–CD scheme," Proc. Combust. Inst. **36**, 2725 (2017).

[59] X. Cai, J. Liang, R. Deiterding, Y. Mahmoudi, and M. Sun, "Experimental and numerical investigations on propagating modes of detonations: Detonation wave/boundary layer interaction," Combust. Flame **190**, 201 (2018).

[60] X. Cai, R. Deiterding, J. Liang, M. Sun, and Y. Mahmoudi, "Diffusion and mixing effects in hot jet initiation and propagation of hydrogen detonations," J. Fluid Mech. **836**, 324 (2017).

[61] H. Peng, Y. Huang, R. Deiterding, Z. Luan, F. Xing, and Y. You, "Effects of jet in crossflow on flame acceleration and deflagration to detonation transition in methane–oxygen mixture," Combust. Flame **198**, 69 (2018).

[62] Y. Wang, W. Han, R. Deiterding, and Z. Chen, "Effects of disturbance on detonation initiation in $H_2/O_2/N_2$ mixture," Phys. Rev. Fluids **3**, 123201 (2018).

[63] V. Bychkov, V. Akkerman, G. Fru, A. Petchenko, and L.-E. Eriksson, "Flame acceleration in the early stages of burning in tubes," Combust. Flame **150**, 263 (2007).

[64] V. Bychkov, M. A. Liberman, and L. Eriksson, "Propagation of curved stationary flames in tubes," Phys. Rev. E **54**, 3713 (1996).

[65] D. Dunn-Rankin and R. F. Sawyer, "The interaction of a laminar flame with its self-cenerated flow during constant volume combustion," in The 10th ICDERS, 1985.

[66] D. Dunn-Rankin and R. F. Sawyer, "Tulip flames: Changes in shape of premixed flames propagating in closed tubes," Exp. Fluids **24**, 130 (1998).

[67] M. Matalon and P. Metzener, "The propagation of premixed flames in closed tubes," J. Fluid Mech. **336**, 331 (1997).

[68] C. Wang, Y. Zhao, and W. Han, "Effect of heat-loss boundary on flame acceleration and deflagration-to-detonation transition in narrow channels," Combust. Sci. Technol. **189**, 1605 (2017).

[69] M. Pöschl and T. Sattelmayer, "Influence of temperature inhomogeneities on knocking combustion," Combust. Flame **153**, 562 (2008).

[70] C. S. Yoo, T. Lu, J. H. Chen, and C. K. Law, "Direct numerical simulations of ignition of a lean n-heptane/air mixture with temperature inhomogeneities at constant volume: Parametric study," Combust. Flame **158**, 1727 (2011).

[71] J. F. Griffith, J. P. MacNamara, C. G. W. Sheppard, D. A. Turton, and B. J. Whitaker, "The relationship of knock during controlled autoignition to temperature inhomogeneities and fuel reactivity," Fuel **81**, 2219 (2002).

[72] M. A. Liberman, M. F. Ivanov, D. M. Valiev, and L. E. Eriksson, "Hot spot formation by the propagating flame and the influence of Egr on knock occurrence in Si engines," Combust. Sci. Technol. **178**, 1613 (2006).

[73] H. Wei, J. Yu, L. Zhou, W. Zhao, and C. Chen, "The LES and LEM study of end-gas auto-ignition mechanism in a downsized spark ignition engine: Effect of turbulence," Combust. Sci. Technol. (published online, 2018).

[74] T. Zhang, W. Sun, L. Wang, and Y. Ju, "Effects of low-temperature chemistry and turbulent transport on knocking formation for stratified dimethyl ether/air mixtures," Combust. Flame **200**, 342 (2019).

[75] L. Chen, H. Wei, C. Chen, D. Feng, L. Zhou, and J. Pan, "Numerical investigations on the effects of turbulence intensity on knocking combustion in a downsized gasoline engine," Energy **166**, 318 (2019).